ACS Catalysis

Research Article

pubs.acs.org/acscatalysis

Density-Functional-Theory Calculation Analysis of Active Sites for Four-Electron Reduction of O_2 on Fe/N-Doped Graphene

Wei Liang, Junxiang Chen, Yuwen Liu, and Shengli Chen*

Hubei Key Laboratory of Electrochemical Power Sources, Key Laboratory of Analytical Chemistry for Biology and Medicine (Ministry of Education), Department of Chemistry, Wuhan University, Wuhan 430072, China

Supporting Information

ABSTRACT: Nanocarbons doped with nitrogen (N) and/or metal-N coordination structures hold great promise in replacing Pt for catalyzing the oxygen reduction reaction (ORR) in fuel cells. The lack of clear views on the natures of ORR active sites in these materials has hindered the progress in reducing their activity gap to Pt through a rational desire of doping structures. Using 14 types of N and Fe−N doping structures in graphene as model systems, systematic density-functional-theory (DFT) calculations are performed within a unified electrochemical thermodynamic framework and the same reaction mechanism to gain insights into ORR active sites in doped nanocarbons. Scaling relations are obtained between the calculated adsorption free energy of key ORR intermediates at surface sites associated with various graphene doping structures. Reaction free energy analysis indicates that the proton−electron transfer coupled O_2 adsorption and/or reduction of adsorbed hydroxyl group (*OH) are the activity-determining steps in the ORR on most doped graphenes and that the ORR activity of various graphene doping structures can be described with a single thermodynamic descriptor, namely, the adsorption free energy of *OH (ΔG_{*OH}). A model volcano plot of ORR activity as a function of ΔG_{*OH} is established for active sites in doped graphenes, which indicates that the surface sites associated with a few edge N-doping structures, such as armchair graphitic N, zigzag pyridinic N, and zigzag pyridinic N oxide, offer optimized binding strength of oxygenated species for catalyzing the ORR. Some other structures, such as in-plane graphitic N and the Fe−N_4 complex and hydrogenated zigzag pyridinic N, are also expected to form ORR activity sites. The possible electronic structure origin of the differing binding strength of oxygenated species on various graphene doping structures is analyzed in terms of the density of p_z states near the Fermi level of active carbon atoms. These results may serve as guidance for designing ORR electrocatalysts of doped nanocarbons. Especially, it is revealed that merely N doping indeed can produce highly active electrocatalytic sites for the ORR in nanocarbons.

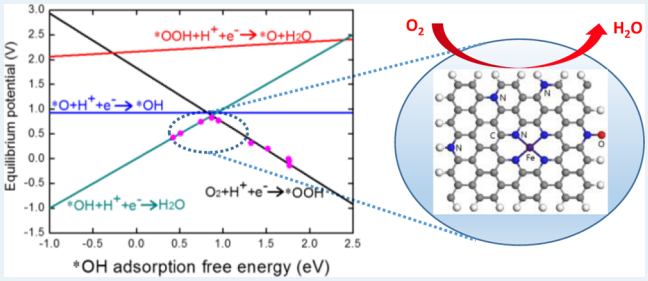

KEYWORDS: *oxygen reduction reaction, doped graphenes, active sites, density functional theory, volcano plot, scaling relationship*

INTRODUCTION

Owing to the high energy efficiency and power density, proton exchange membrane fuel cells (PEMFCs) hold great promise as mobile power sources for low-/zero-emission electric vehicles and as distributed power generators. Current PEMFCs vitally rely on scarce Pt as electrocatalysts. Especially, cathodes in PEMFCs have to be considerably loaded with Pt to overcome the sluggish kinetics of the oxygen reduction reaction (ORR),[1] thus making PEMFCs poorly cost-effective. Great recent efforts have been made to search efficient nonprecious metal ORR electrocatalysts.[2,3] Among various materials explored, nitrogen (N) or metal-N doped nanocarbons have received the most attention. The past few years have evidenced considerable progress in reducing the ORR activity gap between doped nanocarbons and Pt-based materials.[4−13] In these high performance nonprecious metal electrocatalysts, graphenes of different forms, which are introduced as a precursor component or produced through high-temperature (HT) pyrolysis of organic compounds, usually act as the major matrix for heteroatom doping.[4−6,9,11−13] As well as high electric conductivity, graphenes generally possess high specific surface areas, which may counterbalance the low doping density of heteroatoms in carbons. Although graphene-based materials as catalysts for various important reactions have been the subject of extensive recent experimental and theoretical works,[4,5] they remain fairly less active for the ORR than Pt-based electrocatalysts. This, on one hand, is due to the limitation in controlling the doping amounts and structures of heteroatoms in the highly graphitized carbon matrix and, on the other hand and more importantly, is due to the limited knowledge so far gained on the nature of ORR active sites in these materials.[4]

Diverse types of N-containing compounds, such as ammonia, urea, melamine, phenanthroline, polyaniline, polypyrrole, phenylenediamine, etc., have been explored as precursors to

Received: August 11, 2014
Revised: September 29, 2014
Published: October 9, 2014

dope N in graphenes or to grow N-doped graphenes, by using a variety of methods such as simple HT annealing, chemical vapor deposition, solvothermal treatment, or ball milling.[4,5] The resulted materials exhibit a diverse range of doping levels (mostly less than 6 atom %) and structures such as graphitic, pyridinic, and pyrrolic N and metal-N complexes. So far, no conclusive correlation between the ORR activity and the content and distribution of various N and Fe species has been reached, leaving the exact structures of N or metal-N based active sites unclear.[4] For instance, there are considerable works which show materials with a relatively larger amount of graphitic N exhibit higher ORR activity;[14−16] results from some other works tend to suggest that pyridinic and pyrrolic N atoms are responsible for the enhanced ORR activity.[17,18] In addition, it is controversial whether ORR catalytic sites can be formed by merely introducing N in a carbon matrix, or the formation of metal-N coordination structures is necessary. The so-called metal-free electrocatalysts of doped carbons for the ORR have been reported in a considerable number of works;[9,12−19] whereas a large number of studies have shown the necessity of introducing metal for N-doped carbons to become efficient ORR electroctalysts.[6−8,10,11]

Similarly, recent theoretical effort has also produced diverse results and views on ORR electrocatalysis of doped graphenes. Using graphite N as a model doping structure, Boukhvalov and Son[20a] performed systematic density functional theory (DFT) calculations of energetics of various ORR steps on N-doped graphenes with different amounts of nitrogen doping. They showed that for the case of light doped graphene (about 4% of N) the energy barrier for each step is even lower than that for the same process on a platinum surface. Interestingly, more recent calculations by these authors showed that graphite N-doped graphene and graphenes supported over copper could be better electrocatalysts also for the water oxidation reaction than platinum at relatively low temperatures.[20b] Using pyridinic N as the model doping structure, the calculations by Xia and co-workers[21,22] suggested that N doping can introduce high positive spin density and asymmetry atomic charge density, which may be responsible for the enhanced catalytic activity for the ORR. However, the calculations by Ikeda et al.[23] and by Kurak and Anderson[24] seemed to negate pyridinic N as a good doping structure for the ORR. Bao et al.[25] investigated the effect of the location of the graphite N within the graphene cluster on the O_2 chemisorption. They found the zigzag edge doping structure strongly adsorbs O_2 molecules via a "two feet" geometry, which may favor the four-electron ORR. Recent calculations by Gao et al.[26] also implied the importance of edge doping structures. The possibility of using various metal and nonmetal impurity atoms embedded in graphene with defects has also been explored for the ORR by Kaukonen et al.[27] Their calculation results implied that single Ni, Pd, Pt, Sn, and P atoms embedded into divacancies can be good candidates. In addition, there are also several theoretical calculation studies on ORR electrocatalysis at Fe−N coordination structures in graphene-based materials.[28−30] Orellana[28] showed that Fe−N_4 centers in graphene exhibit O_2 dissociation energy which is comparable to that on a Pt (111) surface. However, Zhang et al.[29] showed that an O_2 molecule chemisorbed on the Fe site prefers to be hydrogenated to an adsorbed OOH group rather than directly dissociate. The results by Liu and co-workers[30] gave a similar implication. These authors also showed that the reduction of an adsorbed hydroxyl group (*OH) is the potential-determining step in ORR at Fe−N_4 centers. Baran et al.[31] and Calle-Vallejo et al.[32] have investigated the ORR on metalloporphyrin materials and graphene-based materials containing metal−N_4 structures and showed that there are scaling relationships between the adsorption energies of oxygenated species possibly involved in the ORR, which implied a volcano type of dependence of ORR activity on the binding strength of oxygenated species.

Although a variety of doping structures have been considered in recent theoretical calculation studies on ORR electrocatalysis of graphene-based materials and significant insights have been gained, it is somewhat difficult to compare and correlate the results and conclusions from different studies since the ORR activity has been modeled from very different point of views. For examples, some studies simply considered the adsorption strength of the O_2 molecule. Those considering the full reaction mechanism may have utilized very different reaction and computation schemes. Therefore, a systematic comparison of electrocatalytic properties of various doping structures in graphene under unified reaction and computation schemes is highly expected, which would greatly help identify the most optimized doping structures, so that the graphene-based ORR electrocatalysts can be rationally designed for further activity enhancement. In this study, systematic density functional theory (DFT) calculations are performed within a unified electrochemical thermodynamic framework and reaction scheme to investigate the electrocatalytic activity of various possible N−C and Fe−N−C structures in doped graphenes for the ORR. Surface sites associated with 14 doping structures are considered, including in-plane graphitic N (GN), GN at armchair and zigzag edges (arm-GN and zig-GN), pyridinic N (PyN) at two types of edges (arm-PyN and zig-PyN), hydrogenated PyN at two types of edges (arm-PyN-H and zig-PyN-H), PyN oxide at two types of edges (arm-PyN-O and zig-PyN-O), PyN hydroxide at the armchair edge (arm-PyN−OH), a pyrrolic edge N (pyrrole), and three types of in-plane Fe centers (FeN_4-G, FeN_3-G, and Fe-G). These model structures can be found in Table S1 in the Supporting Information (SI). As has been suggested by XPS and Mössbauer characterization results, theses doping structures could be produced in HT pyrolysis of N-containing compounds or HT doping of N in nanocarbons in the presence/absence of Fe species.[6,10,11,33,34] We first investigate the adsorption of various possible oxygenated intermediates involved in ORR, such as *O_2, *OOH, *O, and *OH, on surface sites associated with above-mentioned doping structures (throughout this paper, the prefix of * means "adsorbed"). The calculated adsorption free energy of these oxygenated intermediates exhibits scaling relationships between each other. The energetics of various possible reaction steps in the ORR are then calculated, based on which the ORR pathways on surface sites associated with different doping structures are evaluated and the steps which determine the ORR activity are identified. Finally, a model volcano plot of the ORR activity as a function of the adsorption free energy of *OH is constructed, on the basis of which the ability of various doping structures to form ORR active sites is discussed.

COMPUTATIONAL DETAILS

Geometry optimization and total energy calculations were performed within DFT framework as implemented with DMol^3 code.[35a] Spin-polarization was considered in all calculations. The PBE exchange-correlation functional within the generalized gradient approximation (GGA)[35b] was adopted. The all-

dx.doi.org/10.1021/cs501170a | ACS Catal. 2014, 4, 4170−4177

electron-relativistic-core method was implemented to treat the relativistic effects. A double numerical basis set was used together with polarization functions (DNP). A smearing of 0.005 Ha (1 Ha = 27.21 eV) to the orbital occupation is applied to achieve accurate electronic convergence. Self-consistent-field (SCF) procedures were performed with a convergence criterion of 1×10^{-6} Ha on the total energy. Geometry optimizations were performed by using the Broyden–Fletcher–Goldfarb–Shanno (BFGS) algorithm.[35c] The convergence tolerances of energy, force, and displacement were 1×10^{-5} Ha, 0.002 Ha/Å, and 0.005 Å, respectively, in the geometry optimization.

Periodical supercells containing single-layer graphenes with a 20 Å vacuum above were used to model various graphene doping structures. For those embedded in the basal plane (in-plane), a periodical graphene slab 9.84 Å × 9.84 Å in size was used, while an armchair edge graphene ribbon 25.61 Å × 8.52 Å in size and a zigzag edge graphene ribbon 9.84 Å × 24.25 Å in size were used to model the corresponding edge structures (Table S1). Each edge structure was separated by ca. 15 Å from its neighbors in ribbon models. The C–C and C–N bond lengths were initially set to 1.42 Å (corresponding to a lattice constant of 2.46 Å) but allowed to relax with adsorbates during the geometric optimization. Periodic graphene slabs and armchair and zigzag graphene ribbons were sampled respectively with 4 × 4 × 1, 1 × 4 × 1, and 4 × 1 × 1 Monkhorst–Pack k-point grids. A conductor-like screening model (COSMO)[35d] was used to simulate the H_2O solvent environment in all calculations. The COSMO is a continuum model in which the solute molecule forms a cavity within the dielectric continuum of permittivity. The dielectric constant was set to 78.54 for H_2O. Using optimized structures obtained within the DMol^3 package, partial density of states (PDOS) of the carbon atom at which *OH is adsorbed in each doping structure are calculated with the Tetrahedron method[36] in the PWscf code included in the QUANTUM-ESPRESSO package.[37]

The computational hydrogen electrode (CHE) model introduced by Nørskov and co-workers[38] was used to calculate the Gibbs free energy of reactions involving electron/proton transfer. In this model, electrode potentials (U) are quoted with respect to the reversible hydrogen electrode (RHE), which makes the standard electrochemical potential of electron involved in reaction (G_e) equal to $-eU$, and the standard electrochemical potential of the proton (G_{H+}) equal to that of the hydrogen atom in gaseous H_2 ($1/2G_{H_2}$). In reaction free energy calculations, entropy values of gaseous molecules were taken from the standard tables in the *Physical Chemistry* text book;[39] zero point energy (ZPE) values of gaseous molecules were estimated from the vibration frequency which are also given in ref 39. ZPE values of the adsorbed species were obtained from DFT calculations using the DMol^3 program, and the entropy of the adsorbed species was ignored. Considering that the high-spin ground state of the O_2 molecule is poorly described in the current DFT scheme, the free energy of the O_2 molecule was derived according to $G_{O_2} = 2G_{H_2O} - 2G_{H_2} + 4 \times 1.23$ (eV). The temperature (T) of 300 K was used in all calculations.

RESULTS AND DISCUSSION

Adsorption of Key Intermediates. We have investigated the adsorption of O_2, OOH, O, and OH at surface sites associated with various graphene doping structures through systematic geometric optimization and total energy calculations, by varying the adsorption sites (Fe, N, and the adjacent carbon atoms) and initial adsorption configuration. The most favored adsorption sites and configurations are given in Table S1 in the SI, and the optimized C–N, C–C, and C–H bonds in the corresponding doping structures before and after adsorption of oxygenated species are given in Table S2. Adsorption free energy values for various oxygenated species (ΔG_{*O_2}, ΔG_{*OOH}, ΔG_{*O}, and ΔG_{*OH}) are calculated as the reaction free energy of $* + 2H_2O \leftrightarrow *O_2 + 2H_2$, $* + 2H_2O \leftrightarrow *OOH + 3/2H_2$, $* + H_2O \leftrightarrow *O + H_2$, and $* + H_2O \leftrightarrow *OH + 1/2H_2$ (* represents surface sites) respectively. The results are given in Table 1. It

Table 1. Gibbs Adsorption Free Energy Values (eV) of Key Oxygenated Intermediates Involved in the ORR on Surface of Various Model Graphene Doping Structures, Calculated As the Free Energy of Reactions Described in Text

doping structures	ΔG_{*O_2}[a]	ΔG_{*OOH}	ΔG_{*O}	ΔG_{*OH}
GN	5.02	4.19	1.49	0.99
zig-GN	4.00	3.97	1.16	0.73
arm-GN	×	4.09	1.78	0.87
zig-PyN	5.22	3.96	2.56	0.74
zig-PyN-H	×	4.72	2.25	1.51
zig-PyN-O	×	4.15	2.49	0.95
arm-PyN	×	4.97	2.72	1.76
arm-PyN-H	4.48	3.70	1.34	0.51
arm-PyN-O	×	4.61	2.59	1.32
arm-PyN–OH	×	5.06	2.92	1.77
pyrrole	×	4.93	2.04	1.76
FeN_4-G	3.84	3.37	1.19	0.42
FeN_3-G	2.17	1.95	−0.41	−0.95
Fe-G	3.38	2.51	0.64	−0.62

[a](×) No stable chemical adsorption configuration was obtained in geometric optimization.

should be pointed out that adsorption free energy values thus calculated do not represent the absolute adsorption strength of each species. Therefore, they should not be used to compare the adsorption strength of different species at the same surface but can be used to predict the trends of adsorption strength of certain species on different sites.

In Figure 1, the calculated adsorption free energy for *OOH and *O (ΔG_{*OOH} and ΔG_{*O}) is plotted as a function of that for *OH (ΔG_{*OH}) on various doping structures. The following linear relationships can be fitted from these data.

$$\Delta G_{*OOH} = (1.1 \pm 0.014)\Delta G_{*OH} + (3.09 \pm 0.016)\text{eV} \quad (1)$$

$$\Delta G_{*O} = (1 \pm 0.08)\Delta G_{*OH} + (0.93 \pm 0.09)\text{eV} \quad (2)$$

The ΔG_{*OOH} vs ΔG_{*OH} data points nicely fall at/near the fitted linear line, with the slope and free energy intercept very similar to that observed on the surface of various metal-based materials ($\Delta G_{*OOH} \approx \Delta G_{*OH} + 3.2$ eV[40,41]). The slope of ca. 1 was believed to be due to *OOH and *OH both adsorbing atop the surface with a single bond between O and a surface atom. In comparison, the ΔG_{*O} vs ΔG_{*OH} data points in Figure 1 show very weak linear correlation, which is different from that on metal-based materials, on which the values of ΔG_{*O} and ΔG_{*OH} also exhibit a fairly reasonable linear relation ($\Delta G_{*O} \approx 2\Delta G_{*OH} - 0.08$ eV[40,41]). In addition, the ΔG_{*O} vs ΔG_{*OH} dependence on doped graphenes considered here exhibits a

dx.doi.org/10.1021/cs501170a | ACS Catal. 2014, 4, 4170–4177

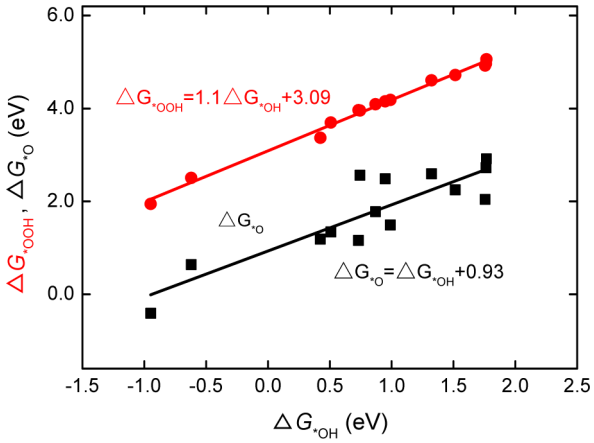

Figure 1. Scaling relations between adsorption free energy values of *OOH and *O and that of *OH at surface sites associated with various graphene doping structures.

different slope from that on the surface metal-based materials. As shown in Table S1, *O adsorbs either at top or bridge sites on the surface of differently doped graphenes, while it mainly adsorbs at hollow sites on the metal surface. We find that data points which significantly deviate from the fitted ΔG_{*O} vs ΔG_{*OH} linear line are mostly given by the bridge-adsorbed *O. Thus, a slope of 1 for the ΔG_{*O} vs ΔG_{*OH} scaling relationship is understandable. Recent DFT calculations by Baran et al.[31] also showed a ΔG_{*O} vs ΔG_{*OH} scaling relationship with a slope of ca. 1 for metalloporphyrin materials.

Scaling relationship between the adsorption free energy of oxygenated intermediates have been shown to be the origin of the large overpotential of the ORR on various electrocatalysts.[40] These relations allow the ORR activity of various materials to be described and compared simply with the adsorption free energy of an oxygenated species, for example, ΔG_{*OH} or ΔG_{*O}.[38,40,41] In present study, we use ΔG_{*OH} due to the relatively poor correlation of ΔG_{*O} with the adsorption free energy of other oxygenated intermediates. As will be shown in the following, the adsorption of *O does not play a determining role in the ORR activity for most of the graphene doping structures considered here, except for Zig-GN and GN, which will be discussed separately. Therefore, ΔG_{*OH} is a more appropriate "descriptor" for the ORR activity for these graphene doping structures.

ORR Pathways. The ORR may proceed through the associative or dissociative pathway, or both of them. The associative and dissociative pathway differ from each other mainly in the initial steps involving the adsorption of O_2. In the associative pathway, the O_2 molecule undergoes either concert or sequential proton−electron transfer (PET)-coupled adsorption to form an *OOH. We will not distinguish the two *OOH formation processes in this study and simply consider the following overall reaction:

$$* + O_2 + H^+ + e^- \leftrightarrow *OOH \quad (R1)$$

In the dissociative pathway, adsorbed oxygen atoms (*O) are formed in the initial adsorption steps. For doping structures which do not give a stable chemisorption state of O_2 in geometric optimization (Table 1 and S1), the ORR should prefer to take place through the *OOH pathway. For those giving a chemisorption state of O_2 in geometric optimization, we have compared the reaction free energy for the associative reaction of the adsorbed $*O_2$, i.e., $*O_2 + H^+ + e^- \leftrightarrow *OOH$, and that for the dissociative reaction of $*O_2$, i.e., $*O_2 \leftrightarrow 2*O$. In addition, we have also computed the activation barriers for the corresponding dissociative reaction of $*O_2$. The results are given in Table 2. The associative reaction free energy is potential dependent. We consider the case at 0.9 V, at which the ORR currents are usually used for a benchmark comparison of various ORR electrocatalysts. The configurations of the dissociated *O atoms are shown in Table S3.

Table 2. Calculated Reaction Free Energy Values (eV) for the Associative (ΔG_a at 0.9 V) and Dissociative (ΔG_d) Reaction of Adsorbed $*O_2$, and the Activation Free Energy Values of the Dissociative Reaction (ΔG_d*)

doping structures	ΔG_a	ΔG_d	ΔG_d*
GN	0.07	0.13	0.28
zig-GN	0.87	−0.23	0.07
zig-PyN	−0.36	−0.71	1.96
arm-PyN-H	0.12	−0.10	0.73
FeN4-G	0.43	0.99	2.39
FeN3-G	0.68	0.38	1.14
Fe-G	0.03	−1.16	1.05

If only reaction free energy values (ΔG_a and ΔG_d) are compared, one would expect that the $*O_2$ dissociation pathway could take place at surface sites in doping structures displayed in Table 2 except for FeN_4-G, at which the associative reaction free energy is much more negative. However, it is also seen that the dissociation of $*O_2$ has considerably high activation barriers for the zig-PyN, FeN_3-G, and Fe-G. The dissociation of $*O_2$ on surface sites in some of these structures (or similar structures) have also been investigated by others. The reported activation energy values were similar to our results.[25,26,42] Thus, it seems that the dissociative pathway may apply only for the GN, zigzag-GN, and arm-PyN-H. As will be shown later on, the steps prior to *O and *OH reduction are very facile and therefore play a minor role in the ORR activity of these structures. Thus, whether $*O_2$ undergoes an associative or dissociative pathway is not important for assessing the ORR activity of these structures.

In the associative pathway, the formed *OOH may undergo the following reactions:

$$*OOH + H^+ + e^- \leftrightarrow *O + H_2O \quad (R2)$$

$$*OOH + H^+ + e^- \leftrightarrow 2*OH \quad (R2a)$$

$$*OOH \leftrightarrow *O + *OH \quad (R2b)$$

$$*OOH + H^+ + e^- \leftrightarrow *H_2O_2 \quad (R2c)$$

Since we are only interested in the four-electron reduction of O_2, the reaction of R2c will not be considered in detail. However, it will be discussed later on for doping structures which are identified as optimized structures for catalyzing the ORR. As will be shown later on, when R2 is involved in the four-electron O_2 reduction, it will be much more facile in thermodynamics than the steps preceding or following it, regardless of doping structures. Therefore, whether R2a and/or R2b are more preferred reactions of *OOH than R2 or not does not affect the identification of the activity-determining step and the analysis of ORR activity for various graphene doping structures. In the case that R2a and R2b are less facile than R2, they would not be involved in the ORR. If they are the

dx.doi.org/10.1021/cs501170a | ACS Catal. 2014, 4, 4170−4177

preferred reaction of *OOH, they should be no doubt much more facile than the preceding *OOH formation step and the following *O and *OH reduction step, thus taking a trivial role in determining the ORR activity.

Activity Volcano Plot and Activity-Determining Steps. To identify the activity-determining step and the relative ORR activity of various graphene doping structures, we first compare the reaction free energy of R1 and R2 and the reduction of *O and *OH, namely, R3 and R4.

$$*O + H^+ + e^- \leftrightarrow *OH \quad (R3)$$

$$*OH + H^+ + e^- \leftrightarrow H_2O \quad (R4)$$

These reaction steps are usually employed to investigate the energetics of the ORR on various materials.[38,29,43,44] The reaction free energy of R1−R4 can be expressed with the adsorption free energy of various oxygenated species defined earlier, which are,

$$\Delta G_1 = \Delta G_{*OOH} - 4.92 + eU \quad (3)$$

$$\Delta G_2 = \Delta G_{*O} - \Delta G_{*OOH} + eU \quad (4)$$

$$\Delta G_3 = \Delta G_{*OH} - \Delta G_{*O} + eU \quad (5)$$

$$\Delta G_4 = -\Delta G_{*OH} + eU \quad (6)$$

Using calculated adsorption free energy values given in Table 1, we can estimate the standard equilibrium potential of each step, U_i^0 (i = 1, 2, 3, or 4), under conditions that $\Delta G_i = 0$. Figure 2 displays the thus obtained U_i^0 values at surface sites in various graphene doping structures. The reaction step which has the lowest (most negative) value for the standard equilibrium potential, which has been termed the potential-determining step,[40,45] represents the thermodynamically least favorable reaction step in the ORR on the interested surface. It has been shown that the potential-determining step usually should be also the rate-determining step in an electrocatalytic reaction.[45] Therefore, we can consider steps which exhibit the lowest standard equilibrium potential in R1−R4 the activity-determining step in the ORR.

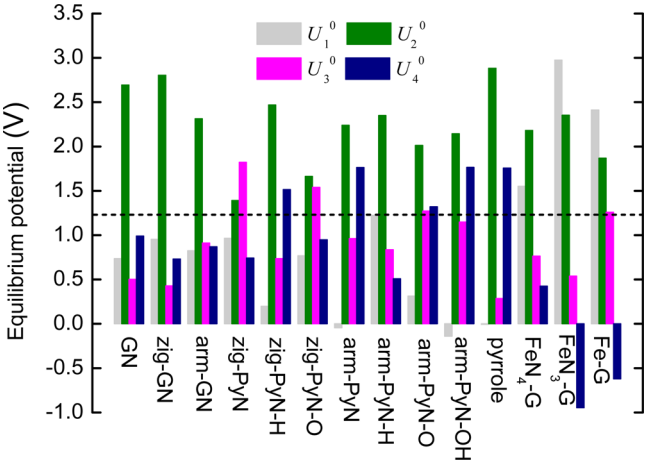

Figure 2. Standard equilibrium potential for reaction steps of R1−R4 in the associative ORR pathway at surface sites in various graphene doping structures, estimated with adsorption free energy values given in Table 1 and eqs 3−6. The black dash line indicates the level of the equilibrium potential for the overall four-electron reduction of ORR in aqueous solution (1.23 V).

As seen in Figure 2, all doping structures considered here give U_2^0 values (green bars) which are more positive than the equilibrium potential for the overall four-electron ORR in aqueous solution (1.23 V), indicating that R2 is a very facile step in the ORR. Except that at surface sites in GN and zig-GN, either R1 or the R4 has the lowest values of standard equilibrium potential. This tells that the activity-determining step in the ORR at surface sites in these graphene doping structures is either R1 or R4.

According to the scaling relationship between the adsorption free energy of various intermediates fitted in Figure 1, U_i^0 can be related to ΔG_{*OH} according to eqs 7−10.

$$eU_1^0 = 1.83 - 1.1\Delta G_{*OH} \quad (7)$$

$$eU_2^0 = 0.1\Delta G_{*OH} + 2.16 \quad (8)$$

$$eU_3^0 = 0.93 \quad (9)$$

$$eU_4^0 = \Delta G_{*OH} \quad (10)$$

In Figure 3, U_i^0 values for the activity-determining steps shown in Figure 2 and that predicted by eqs 7−10 are plotted against the corresponding ΔG_{*OH} given in Table 1. It can be seen that model relations of U_i^0 vs ΔG_{*OH} given by eqs 7−10 also predict activity-determining steps of R1 and/or R4. At surface sites which bind oxygenates weakly (have relatively positive ΔG_{*OH}), U_1^0 would have the lowest value, while U_4^0 is the lowest in value at surface sites where the oxygenates are strongly bonded. In the case when U_1^0 determines the overpotential of the ORR, the decrease in ΔG_{*OH} (increasing the *OH binding strength) would result in lowered ORR overpotential. On the contrary, lowering the ORR overpotential requires decreasing the *OH binding strength as U_4^0 determines the overpotential. As a result, the lowest ORR overpotential will be achieved at an intermediate *OH adsorption strength at which the U_1^0 vs ΔG_{*OH} and U_4^0 vs ΔG_{*OH} curves cross with each other. Thus, the U_1^0 vs ΔG_{*OH}

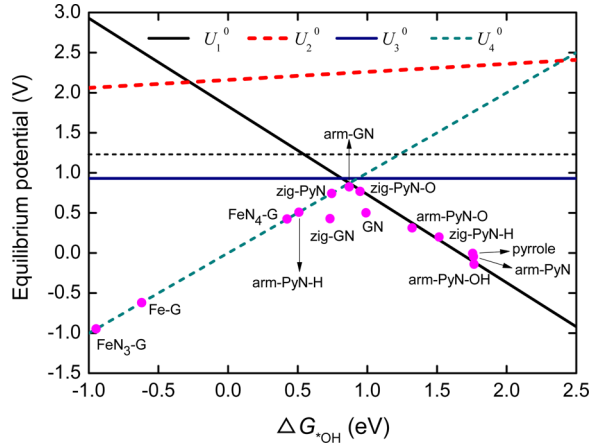

Figure 3. Thermodynamic volcano relation for ORR activity as a function of *OH binding strength at surface sites in various graphene doping structures. Magenta data points are the calculated standard equilibrium potential for the potential-determining step. The lines of different styles and colors are the U_i^0 vs ΔG_{*OH} dependence predicted by eqs 7−10 which are derived according to the scaling relations between the adsorption free energy of various intermediates. The black dash line indicates the level of the equilibrium potential for the overall four-electron reduction of ORR in aqueous solution (1.23 V).

dx.doi.org/10.1021/cs501170a | ACS Catal. 2014, 4, 4170−4177

curve in the weak bonding region and the U_4^0 vs ΔG_{*OH} curve in the strong bonding region form a thermodynamic activity volcano plot for the ORR.

According to eqs 7 and 10, the volcano top should appear at ΔG_{*OH} values around 0.8 V, at which $U_1^0 = U_4^0 = \Delta G_{*OH}$. It is noticed that the activity volcano plot for the ORR derived from the scaling relationship for oxygenated intermediates on the surface of metal electrocatalysts also exhibit a standard equilibrium potential value of ca. 0.8 V in the top region.[40] Therefore, this standard equilibrium potential value for the activity-determining steps should correspond to the best achievable ORR activity in the thermodynamic viewpoint. Please note that the calculated standard equilibrium potential of the activity-determining steps are not the onset potential of the ORR. This is because the coverage of oxygenated intermediates under real ORR conditions should be much different from that assumed in calculating the standard equilibrium potential. To help understand this, one can consider the steady-state polarization curve associated with a simple redox reaction, which could exhibit a half-wave potential close to the standard equilibrium potential.[46] In addition, at ΔG_{*OH} values at which the ORR activity reached the volcano top, U_1^0, U_3^0, and U_4^0 are comparable in values (Figure 3). In this case, the ORR activity should be determined simultaneously by steps of R1, R3, and R4, rather than by a single step. More detailed models are required to relate the ORR activity with ΔG_{*OH} and the standard equilibrium potential of the activity-determining steps. However, this should not prevent us from identifying ORR active doping structures from the volcano plot in Figure 3.

Doped Graphenes As ORR Electrocatalysts. As shown in Figure 3, the surface sites in doping structures of arm-PyN-H, FeN_4-G, Fe-G, and FeN_3-G fall in the strong bonding branch, suggesting that they are too oxophilic to catalyze the ORR. As for the surface sites in doping structures of arm-PyN-OH, arm-PyN, pyrrole, and zig-PyN-H, they are too less oxophilic to act as ORR catalytic centers. Doping structures of arm-GN, zig-PyN-O, and zig-PyN are at or near the volcano top, which implies that they offer the most optimized binding strength of oxygenated species for catalyzing the ORR. Considering that the activity volcano plot in Figure 3 exhibits very similar standard equilibrium potential values in the top region to that obtained for metal-based electrocatalysts,[40] it is expected that doping structures of arm-GN, zig-PyN-O, and zig-PyN could catalyze the ORR as efficiently as surface sites on Pt-based materials. It should be emphasized that, although individual catalytic sites in these doping structures could be as efficient as surface sites on Pt, the limited doping of heteroatoms in graphitized carbons would make the number density of catalytic sites on graphene-based electrocatalysts much lower than that on the Pt surface. Therefore, the mass activity of doped graphenes for ORR would remain much less competitive as compared with Pt-based materials. To this end, synthetic strategies for controlling the edge doping structures and increase doping density of those identified structures are highly expected.

Although doping structures of GN, zig-GN, arm-PyN-H, and FeN_4-G are not located in the top region of the volcano plot, they should still produce considerable ORR activity since the corresponding standard equilibrium potential does not deviate significantly from those near the top. For doping structures of zig-GN and GN, the lowest standard equilibrium potential is given by R3. Therefore, their data points do not fall on either branch of the volcano plot. In fact, they do not fall on the U_3^0 vs ΔG_{*OH} line either. This is because the data for fitting the scaling relationship of ΔG_{*O} vs ΔG_{*OH} are considerably dispersive (Figure 1). As pointed out in the previous section, the ORR may proceed through the dissociative pathway at surface sites in these structures. According to the calculated free energy, R3 for these structures is less facile in thermodynamics than R1. Since the O_2 dissociation step for these structures is even more facile than R1, R3 should be also the thermodynamically least favorable step if the dissociative pathway applies.

We have attempted to investigate the possibility for the formation of H_2O_2 through proton-coupled electron transfer to *OOH (reaction R2c) at surface sites associated with doping structures which are located at/near the top of the activity volcano plot, namely, arm-GN, zig-PyN-O, and zig-PyN, and the doping structure of FeN_4-G. When performing geometry optimization for the adsorbed H_2O_2, it spontaneously dissociates into an *O and a H_2O molecule. This implies that the H_2O_2 reaction pathway unlikely occurs on these ORR active structures.

Possible Electronic Structure Origin of Oxophilicity of Graphene Doping Structures. It is now clear that the ORR activity of graphene doping structures is mainly determined by the binding strength of oxygenated species. Doping structures which have an optimized binding ability to oxygenated species will be more active than those binding oxygenated species too strong or too weakly. To understand the differing oxophilicity of various graphene doping structures, we have performed preliminary electronic structure calculations for carbon atoms which participate in the adsorption of oxygenated species in some representative doping structures. It is found that the trends in the binding strength of oxygenated species can be correlated with the density of p_z states near the Fermi level. The doping structure which has a higher density of p_z states binds oxygenated species stronger. This is manifested in Figure 4, which shows the calculated partial density of states (PDOS) of the carbon atom at which *OH is adsorbed in three doping structures, namely, arm-PyN-H, arm-GN, and arm-PyN−OH. These structures are located at the strong adsorption branch, top, and weak adsorption branch of the activity volcano plot, respectively.

As shown in Figure 4, electronic states near the Fermi level of active carbon atoms in various graphene doping structures are predominately contributed by the p_z orbital. The doping structure of arm-PyN-H, which binds *OH fairly strong as indicated in Figure 3, exhibits the largest DOS near the Fermi level among the three structures considered in Figure 4, whereas the structure of arm-PyN-OH, which binds *OH very weakly, exhibits greatly diminished Fermi DOS. For the doping structure of arm-GN that has moderate oxophilicity, the Fermi DOS is lower than that in arm-PyN-H. Such correlation seems to suggest that p_z orbitals in the corresponding carbon atoms participate in bonding the adsorbed oxygenated species. In graphenes, p_x and p_y orbitals in each carbon atom undergo sp^2 hybridization to form σ bonds with neighboring atoms along the graphene plane. Therefore, it is easy to understand that the p_z orbital in a carbon atom, which is perpendicular to the graphene plane, would be the major orbital participating in the bonding interaction with molecules that adsorb on the surface. The higher density of p_z states should result in enhanced bonding interaction. More detailed electronic structure calculation and analysis are required to quantitatively understand the trends in the binding ability of graphene doping structures to oxygenated species. This may be beyond the scope

dx.doi.org/10.1021/cs501170a | ACS Catal. 2014, 4, 4170−4177

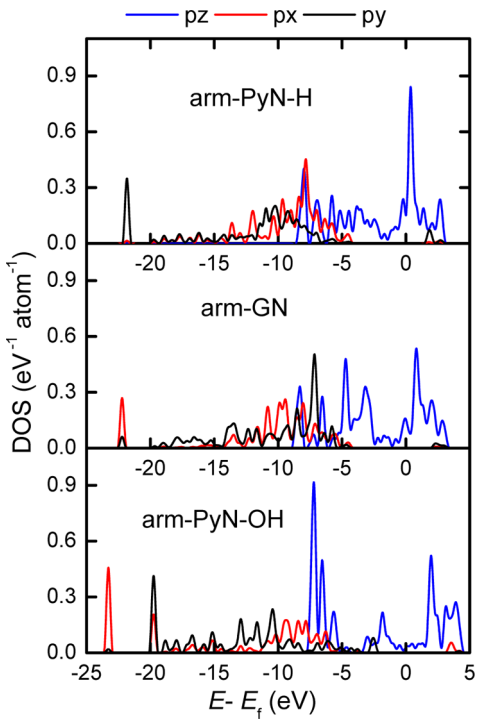

Figure 4. Calculated partial density of states (PDOS) of the carbon atom at which *OH is adsorbed in three doping structures, namely, arm-PyN-H, arm-GN, and arm-PyN−OH, which are located at the strong adsorption branch, top, and weak adsorption branch of the activity volcano plot (Figure 3), respectively.

of the present paper since here we are mainly interested in how the binding ability to oxygenated species may affect the ORR activity of various doping structures and what type of doping structures would produce highly active catalytic sites for the ORR.

CONCLUSION

The electrocatalytic activity of various possible N−C and Fe−N−C centers in doped graphenes for the ORR has been investigated by performing systematic DFT calculations within a unified electrochemical thermodynamic framework and reaction mechanism. The main results and conclusions gained from the calculations are as follows:

(1) The electrocatalytic activity of various doping structures for the ORR in most cases is determined by the reaction steps of the proton−electron transfer coupled O_2 adsorption and/or the reduction of adsorbed *OH.

(2) At surface sites in various doping structures, the adsorption free energy values of key oxygenated intermediates in ORR, such as *OOH, *O, and *OH, approximately linearly scale with each other. This makes the ORR activity of various graphene doping structures can be described with a single thermodynamic descriptor, namely, the adsorption free energy of an oxygenated species, e.g., *OH.

(3) The scaling relations cause the ORR activity of doped graphenes not to simply increase or decrease with their binding ability to oxygenated species but instead to exhibit a volcano type of dependence on the binding ability to oxygenated species.

(4) According to the model volcano plot of ORR activity as a function of the adsorption free energy of *OH, surface sites in a few edge N-doping structures, such as armchair graphitic N, zigzag pyridinic N, and zigzag pyridinic N oxide, may offer optimized strength of oxygenated species for catalyzing ORR.

(5) Electronic structure calculations suggest that the trends in the binding strength of oxygenated species can be correlated with the density of p_z states near the Fermi level of doping structures. Those have a higher density of p_z states bind oxygenated species stronger.

These results and conclusions would throw new insights into the nature of ORR active sites at graphene-based nonprecious metal electrocatalysts and may serve as guidance for rationally material design. More importantly, it is suggested that merely N doping can produce highly active electrocatalytic sites for ORR in nanocarbons and that the edge doping structures are vitally important for nanocarbons to be as active as Pt for the ORR. Therefore, synthetic strategies for controlling the edge doping structures and increasing the doping density of identified doping structures are highly expected.

ASSOCIATED CONTENT

Supporting Information

Geometric data and results in optimized structures (adsorption sites and configurations and bond lengths). This material is available free of charge via the Internet at http://pubs.acs.org.

AUTHOR INFORMATION

Corresponding Author

*E-mail: slchen@whu.edu.cn.

Notes

The authors declare no competing financial interest.

ACKNOWLEDGMENTS

This work was supported by the Ministry of Science and Technology of China under the National Basic Research Program (Grant Nos. 2012CB215500 and 2012CB932800) and the National Natural Science Foundation of China (Grant No. 21073137).

REFERENCES

(1) Gasteiger, H. A.; Markovic, N. M. *Science* **2009**, *324*, 48−49.
(2) Chen, Z.; Higgins, D.; Yu, A. P.; Zhang, L.; Zhang, J. *Energy Environ. Sci.* **2011**, *4*, 3167−3192.
(3) Wang, D. W.; Su, D. S. *Energy Environ. Sci.* **2014**, *7*, 576−591.
(4) Kong, X. K.; Chen, C. L.; Chen, Q. W. *Chem. Soc. Rev.* **2014**, *43*, 2841−2857.
(5) Navalon, S.; Dhakshinamoorthy, A.; Alvaro, M.; Garcia, H. *Chem. Rev.* **2014**, *114*, 6179−6212.
(6) Wu, G.; More, K. L.; Johnston, C. M.; Zelenay, P. *Science* **2011**, *332*, 443−447.
(7) Lefevre, M.; Proietti, E.; Jaouen, F.; Dodelet, J. P. *Science* **2009**, *324*, 71−74.
(8) Gong, K.; Du, F.; Xia, Z.; Durstock, M.; Dai, L. *Science* **2009**, *323*, 760−764.
(9) Wei, W.; Liang, H.; Parvez, K.; Zhuang, X.; Feng, X.; Mullen, K. *Angew. Chem., Int. Ed.* **2014**, *53*, 1570−4.
(10) Wang, Q.; Zhou, Z. Y.; Lai, Y. J.; You, Y.; Liu, J. G.; Wu, X. L.; Terefe, E.; Chen, C.; Song, L.; Rauf, M.; Tian, N.; Sun, S. G. *J. Am. Chem. Soc.* **2014**, *136*, 10882−10885.
(11) Zhang, S. M.; Zhang, H. Y.; Liu, Q.; Chen, S. L. *J. Mater. Chem. A* **2013**, *1*, 3302−3308.
(12) Qu, L. T.; Liu, Y.; Baek, J. B.; Dai, L. M. *ACS Nano* **2010**, *4*, 1321−1326.
(13) Jiao, Y.; Zheng, Y.; Jaroniec, M.; Qiao, S. Z. *J. Am. Chem. Soc.* **2014**, *136*, 4394−403.
(14) Geng, D.; Chen, Y.; Li, Y.; Li, R.; Sun, X.; Ye, S.; Knights, S. *Energy Environ. Sci.* **2011**, *4*, 760−764.

(15) Lin, Z.; Waller, G. H.; Liu, Y.; Liu, M.; Wong, C. P. *Nano Energy* **2013**, *2*, 241−248.
(16) Niwa, H.; Horiba, K.; Harada, Y.; Oshima, M.; Ikeda, T.; Terakura, K.; Ozaki, J. I.; Miyata, S. *J. Power Sources* **2009**, *187*, 93−97.
(17) Lai, L.; Potts, J. R.; Zhan, D.; Wang, L.; Poh, C. K.; Tang, C.; Gong, H.; Shen, Z.; Lin, J.; Ruoff, R. S. *Energy Environ. Sci.* **2012**, *5*, 7936−7942.
(18) Ding, W.; Wei, Z. D.; Chen, S. G.; Qi, X. Q.; Yang, T.; Hu, J. S.; Wang, D.; Wan, L. J.; Alvi, S. F.; Li, L. *Angew. Chem., Int. Ed.* **2013**, *52*, 1−6.
(19) Saidi, W. A. *J. Phys. Chem. Lett.* **2013**, *4*, 4160−4165.
(20) (a) Boukhvalov, D. W.; Son, Y. W. *Nanoscale* **2012**, *4*, 417−420. (b) Boukhvalov, D. W.; Son, Y. W.; Ruoff, R. S. *ACS Catal.* **2014**, *4*, 2016−2021.
(21) Zhang, L.; Niu, J.; Dai, L.; Xia, Z. *Langmuir* **2012**, *28*, 7542−7550.
(22) Zhang, L.; Xia, Z. *J. Phys. Chem. C* **2011**, *115*, 11170−11176.
(23) Ikeda, T.; Boero, M.; Huang, S. F.; Terakura, K.; Oshima, M.; Ozaki, J. I. *J. Phys. Chem. C* **2008**, *112*, 14706−14709.
(24) Kurak, K. A.; Anderson, A. B. *J. Phys. Chem. C* **2009**, *113*, 6730−6734.
(25) Bao, X. G.; Nie, X. W.; von Deak, D.; Biddinger, E.; Luo, W. J.; Asthagiri, A.; Ozkan, U.; Hadad, C. *Top. Catal.* **2013**, *56*, 1623−1633.
(26) Gao, F.; Zhao, G. L.; Yang, S. Z. *ACS Catal.* **2014**, *4*, 1267−1273.
(27) Kaukonen, M.; Krasheninnikov, A. V.; Kauppinen, E.; Nieminen, R. M. *ACS Catal.* **2013**, *3*, 159−165.
(28) Orellana, W. *J. Phys. Chem. C* **2013**, *117*, 9812−9818.
(29) Zhang, J.; Wang, Z. J.; Zhu, Z. P. *J. Power Source* **2014**, *255*, 65−69.
(30) Sun, J.; Fang, Y. H.; Liu, Z. P. *Phys. Chem. Chem. Phys.* **2014**, *27*, 13733−13740.
(31) Baran, J. D.; Gronbeck, H.; Hellman, A. *J. Am. Chem. Soc.* **2014**, *136*, 1320−1326.
(32) Calle-Vallejo, F.; Martinez, J. I.; Rossmeisl, J. *Phys. Chem. Chem. Phys.* **2011**, *34*, 15639−43.
(33) Li, W. M.; Wu, J.; Higgins, D. C.; Choi, J. Y.; Chen, Z. W. *ACS Catal.* **2012**, *2* (12), 2761−2768.
(34) Holby, E. F.; Wu, G.; Zelenay, P.; Taylor, C. D. *J. Phys. Chem. C* **2014**, *118* (26), 14388−14393.
(35) (a) Delley, B. *J. Chem. Phys.* **1990**, *92*, 508. (b) Perdew, J. P.; Burke, K.; Ernzerhof, M. *Phys. Rev. Lett.* **1996**, *77*, 3865−3868. (c) Broyden, C. G. *IMA J. Appl. Math.* **1970**, *6*, 76−90. (d) Klamt, A.; Schüürmann, G. *J. Chem. Soc. Perkin. Trans.* **1993**, *2*, 799−805.
(36) Blöchl, P. E.; Jepsen, O.; Andersen, O. K. *Phys. Rev. B* **1994**, *49*, 16223−16233.
(37) Giannozzi, P.; Baroni, S.; Bonini, N.; Calandra, M.; Car, R.; Cavazzoni, C.; Ceresoli, D.; Chiarotti, G. L.; Cococcioni, M.; Dabo, I.; Dal Corso, A.; de Gironcoli, S.; Fabris, S.; Fratesi, G.; Gebauer, R.; Gerstmann, U.; Gougoussis, C.; Kokalj, A.; Lazzeri, M.; Martin-Samos, L.; Marzari, N.; Mauri, F.; Mazzarello, R.; Paolini, S.; Pasquarello, A.; Paulatto, L.; Sbraccia, C.; Scandolo, S.; Sclauzero, G.; Seitsonen, A. P.; Smogunov, A.; Umari, P.; Wentzcovitch, R. M. *J. Phys.: Condens. Matter* **2009**, *21*, 395502.
(38) Norskov, J. K.; Rossmeisl, J.; Logadottir, A.; Lindqvist, L.; Kitchin, J. R.; Bligaard, T.; Jonsson, H. *J. Phys. Chem. B* **2004**, *108*, 17886−17892.
(39) Atkins, P. W.; Paula, J. *Physical Chemistry*, 9th ed.; Oxford University Press: Oxford, U.K., 2010; pp 472, 922, 924, 933.
(40) Koper, M. T. M. *J. Electroanal. Chem.* **2011**, *660*, 254−260.
(41) Man, I. C.; Su, H. Y.; Calle-Vallejo, F.; Hansen, H. A.; Martinez, J. I.; Inoglu, N. G.; Kitchin, J.; Jaramillo, T. F.; Norskov, J. K.; Rossmeisl, J. *ChemCatChem.* **2011**, *3*, 1159−1165.
(42) Yu, L.; Pan, X. L.; Cao, X. M.; Hu, P.; Bao, X. H. *J. Catal.* **2011**, *282*, 183−190.
(43) Gao, F.; Zhao, G. L.; Yang, S. Z.; Spivey, J. J. *J. Am. Chem. Soc.* **2013**, *135*, 3315−3318.
(44) Lee, D. H.; Lee, W. J.; Lee, W. J.; Kim, S. O.; Kim, Y. H. *Phys. Rev. Lett.* **2011**, *106*, 175502.
(45) Koper, M. T. M. *J. Solid State Electrochem.* **2012**, *17*, 339−344.
(46) Bard, A. J. F. L. R. In *Electrochemical Methods: Fundamentals and Applications*; John Wiley & Sons: New York, 2001; pp 176−204.